Ground based hyperspectral imaging for extensive mango yield estimation

Salvador Gutiérrez[a,*], Alexander Wendel[b], James Underwood[b]

[a]*Instituto de Ciencias de la Vid y del Vino (University of La Rioja, CSIC, Gobierno de La Rioja), Finca La Grajera, Ctra. Burgos Km. 6, 26007 Logroño, Spain*
[b]*Australian Centre for Field Robotics, The Rose Street Building J04, The University of Sydney, NSW 2006, Australia*

Abstract

Fruit yield estimation in orchard blocks is an important objective in the context of precision agriculture, as it makes it easier for the farmer to plan ahead and efficiently use resources. Nevertheless, its implementation is labour-intensive and involves the manual counting of the fruit present in the trees. While colour (RGB) has been widely shown to be successful and arguably sufficient for yield estimation in orchards, hyperspectral imaging (HSI) shows promise for more nuanced tasks such as disease detection, cultivar classification and fruit maturity estimation. Therefore, it is important to ask how appropriate is HSI for the task of yield estimation, with a view to performing all of these tasks with just one sensor. This paper presents a novel mango yield estimation pipeline using ground based line-scan HSI acquired from an unmanned ground vehicle. Hyperspectral images were collected on a commercial mango orchard block in December 2017 and pre-processed for illumination compensation. After tree delimitation and mango pixel identification, an optimisation process was carried out to obtain the best models for fruit counting, using mango counts obtained by manually counting the fruit on-tree, and using state-of-the-art RGB techniques for yield estimation. Models were validated and tested on hundreds of trees, and subsequently mapped. In testing, determination coefficients reached values of up to 0.75 against field counts (predicting 18 trees) and 0.83 against RGB mango counts (predicting 216 trees). These results suggest that line-scan HSI can be used to accurately estimate yield in orchards, especially in scenarios in which this technology is already chosen for the determination of other traits.

Keywords: fruit counting, field robotics, computer vision, lidar, hyperspectral

1. Introduction

Fruit yield estimation is a sought key objective for the precise management in orchard blocks, and it would also be more useful if performed several times within the growing season. Nonetheless, its current practice—involving labour-intensive tree sampling, manual counting and extrapolation—becomes virtually infeasible to be considered as an efficient tool in the decision making process (Payne et al., 2013). Furthermore, even if performed, the accuracy of manual counting is greatly decreased by the fact that yield variability can be very high between trees, so the correct spatial representation of fruit yield distribution is difficult to

*Corresponding author
Email addresses: salvador.gutierrez@unirioja.es (Salvador Gutiérrez), a.wendel@acfr.usyd.edu.au (Alexander Wendel), j.underwood@acfr.usyd.edu.au (James Underwood)

measure (Anderson et al., 2018). The use of different types of sensors for fruit detection can be found in several studies (Gongal et al., 2015), and computer vision has emerged as the most popular choice (Payne and Walsh, 2014). In the case of mango orchards, standard cameras have been used by Payne et al. (2013); Qureshi et al. (2017) for fruit counting, and Wang et al. (2017) made use of three different depth cameras for the estimation of mango size. Additionally, Stein et al. (2016) demonstrated the possibility of applying multiple view geometry to identify and track every piece of fruit in mango orchards. The accuracy of RGB cameras has thus been extensively demonstrated for in-field mango counting and yield estimation, and is arguably sufficient for this application.

Beyond yield estimation, it is also desirable to measure traits such as disease and stress, maturity and nutritional status, for which sensors other than RGB show promise. Hyperspectral imaging (HSI), due to its great potential and capability of characterise multiple objective traits, has been extensively studied and used for many food and agricultural applications (Sun, 2010; Park and Lu, 2015). This technology takes advantage of both spectral and spatial spaces, combining the powerful and demonstrated prediction effectiveness of spectroscopy analysis and the high amount of information that two-dimensional images cover. Uses of HSI have been reported for the monitoring of fruit in apples (Tian et al., 2018; Ma et al., 2018); mangoes (Pu and Sun, 2015; Rungpichayapichet et al., 2017); or grapes (Diago et al., 2016; Gomes et al., 2017), and in plants for disease control (Lu et al., 2017; Thomas et al., 2018); nutritional status assessment (Wang et al., 2018; Zhou et al., 2018); and varietal classification (Diago et al., 2013; Guo et al., 2017). All these works exemplify how HSI can be considered as a promising and useful technology to take over the tasks that are usually assigned to many other destructive, time-consuming procedures.

While many HSI studies were performed under controlled indoor laboratory conditions, it has been demonstrated in recent years that HSI can be performed in field conditions also. Some examples are found in studies using HSI from satellites or aerial platforms (Yang et al., 2004; Oldeland et al., 2010; Zhang et al., 2013), and more recently mounting hyperspectral cameras on unmanned aerial vehicles (UAVs) for a closer range monitoring (Uto et al., 2013; Yue et al., 2017; Ishida et al., 2018). Although UAVs can rapidly cover large areas, they usually offer low resolution when measuring all relevant elements from the target. For this reason, ground based HSI arises as an useful alternative to provide high resolution data while still retaining the ability of extensive, rapid monitoring. Some studies have recently displayed the deployment of hyperspectral cameras on mobile ground-vehicle platforms under field conditions. Deery et al. (2014) reported the use of HSI among other sensors on man-driven buggies, while Gutiérrez et al. (2018) demonstrated the suitability of on-the-go HSI for varietal classification. Moreover, fully autonomous robots equipped with multiple sensors (including a hyperspectral camera) have been successfully developed by Wendel and Underwood (2016) or Underwood et al. (2017), while the authors have also refined the reliability of outdoor hyperspectral data, subjected to changing illumination conditions (Wendel and Underwood, 2017b), and for accurate mapping (Wendel and Underwood, 2017a). Therefore, ground based HSI and its wide range of applications becomes a powerful tool to be applied in precision agriculture.

Considering the practical deployment of an orchard mapping system with minimal sensors, it is therefore important to ask how appropriate is HSI alone for the task of yield estimation, as an alternative to RGB cameras. RGB is arguably good enough, but HSI offers advantages for estimating additional nuanced traits. If the latter are required in addition to yield estimation, a simpler system would aim to do both tasks with

the one sensor. Because, to the best of our knowledge, no prior work exists on yield estimation using ground based HSI, we therefore wish to answer the question, what is the performance of line-scan HSI for yield estimation compared to a state-of-the-art RGB approach? The full spectral information in HSI data should be better per-pixel than RGB for detecting fruit, as there is significantly more information in each pixel, though modern RGB fruit detection methods (*e.g.*, neural networks) also rely on contextual information which may be more important than pixel colour. Though superior information is available in each pixel, line-scan HSI sensors commonly make significant sacrifices in the spatial dimension compared to RGB cameras, with lower resolution and/or limited fields of view, which would make them less suitable. This is particularly problematic considering the success of modern approaches based on convolutional neural networks, which explicitly consider spatial structure within the data (Bargoti et al., 2015; Bargoti and Underwood, 2017) and the use of multiple view geometry to mitigate occlusion of hidden fruit (Stein et al., 2016).

The objective of this paper was to evaluate the performance of line scan, ground based HSI for the task of mango yield estimation, as this technology has not yet been used for this task, to the best of our knowledge. This work breaks new ground both by developing a pipeline that is appropriate for the end-to-end task where none previously existed, and comprehensively evaluating the performance compared to state of the art RGB techniques at whole-orchard scale. We therefore present new knowledge to orchard mapping system designers in two forms: first, how well does HSI imaging work compared to state of art RGB approaches, to answer whether the trade-off is acceptable; and second, a validated implementation for the processing pipeline.

2. Materials and methods

The sequential steps in the proposed method form a pipeline as shown in Fig. 1. In summary: in-field HSI of mango trees was performed in an commercial orchard block by an unmanned ground vehicle platform; spectral pre-processing was applied for illumination compensation; trees were delimited using a complimentary LIDAR segmentation method; mango pixels were identified by classifying the spectra and clusters of connected fruit pixels were segmented to individual fruit using morphological operations; an optimisation procedure was designed to obtain the best the parameters for fruit counting; results were validated with field counts and fruit counts from an RGB baseline approach and they were finally mapped.

Mango yield ground truth values (*i.e.*, the number of mangoes present in each tree) were required in the optimisation and validation steps. These were provided from two different procedures: manual mango field counts (a person in the orchard counting fruit in the tree) and state-of-the-art RGB machine vision mango counts (from Stein et al. (2016)). The processing pipeline for mango yield estimation using HSI remained the same regardless of the ground truth values used.

2.1. Data collection

Data were collected during the 6th and 7th December 2017 in a mango (*Mangifera indica* L.) commercial orchard block (cultivar B74) from Simpson Farms, located in Bundaberg, Queensland, Australia. Ten tree rows were measured, with lengths ranging from 58 m to 260 m, comprising a total of 494 trees. The full dataset was split into five different subsets, described in Table 1. The specific tree assignments are displayed in Fig. 2. Field count data were collected by manually counting on-tree mangoes.

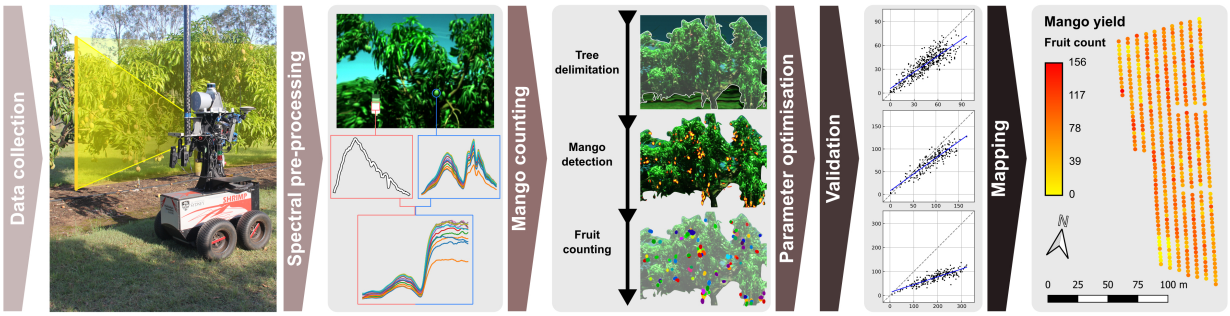

Figure 1: Workflow of the methodology applied in this paper. Hyperspectral imaging was collected by an unmanned ground vehicle; followed by spectral pre-processing; tree delimitation; mango detection and fruit counting; optimisation and validation; and finally mapping.

Table 1: Subset used in the study described in this paper.

Dataset name	Number of trees	Purpose
Field count train	27	Optimisation with field count data
Field count test	18	Testing against independent field count data
RGB train	18	Optimisation with RGB fruit counts
RGB validation	215	Validation of the optimisation results
RGB test	216	Testing against external RGB fruit count data

The data were subdivided into five subsets. The reader is also referred to Fig. 2. The total number of trees in the orchard is 494. RGB fruit counts were obtained following the procedure by Stein et al. (2016). Field count data were obtained by manually counting the visible mangoes still on the tree.

The spectral data were acquired using an unmanned ground vehicle (UGV) developed at the Australian Centre for Field Robotics, called Shrimp. The platform was equipped with a Resonon Pika II Vis-NIR hyperspectral line-scan camera (Resonon, Inc., Bozeman, USA), a Velodyne HDL64E 3D light detection and ranging (LIDAR) (Velodyne LiDAR Inc., San José, USA) and a Novatel SPAN-CPT real time kinematic GPS and inertial navigation system with RTK correction (NovAtel Inc., Calgary, Canada). The camera acquires a single line of 648 spatial pixels, each one of them containing a spectra of 244 datapoints with a bit depth of 12, covering the range from approximately 390 to 890 nm (spectral resolution of 2 nm). It was mounted to the platform to cast a vertical measurement line for a push-broom hyperspectral image composition (by the platform's motion) at 133 frames per seconds. A 6 mm objective lens (43.5º of field of view–FOV) was installed to the camera and manually focused with a checker board at a measurement distance of 2 m. On average, this distance was maintained during continuous data acquisition. With the described FOV and distance, the vertical line covered a height of approximately 1.6 m upon the trees. The LIDAR sensor was mounted sideways for a complete tree height measurement, and set for a 10 Hz spin rate, taking 1.3 million points per second.

The spectral data was taken from both the east and west side of the mango tree rows, traversing the lanes with a continuous data acquisition at 5 km/h. The UGV was configured to make a complete measurement

Figure 2: Orchard block used in data collection, comprising a total of 494 trees. The complete tree dataset was split into five subsets comprising 27, 18, 18, 215 and 216 trees, respectively. The reader is also referred to Table 1. Orthoimagery was collected from *Google Maps*.

run of the whole orchard in a single run, without stopping, other than to turn at the headland. Each row side was measured assuring that the sun was directly lighting the trees from behind the camera. Therefore, the east side acquisitions were performed in the morning, and west side in the afternoon. Illumination reference panels (QPcard 102) were mounted on tripods and placed at several sunlit and shaded points in the field to cover a wide range of reference illumination conditions. Likewise, dark current measurements were taken in a regular basis, by covering the sensor lens and acquiring data for 10 s. Concurrently to HSI acquisition, RGB images were also acquired at 5 Hz using a Prosilica GT3300C camera (Allied Vision Technologies GmbH, Stadtroda, Germany) synchronised to four Excelitas MVS-5002 strobe lights (Excelitas Technologies Corp., Waltham, USA). Full details about RGB acquisition can be found in Stein et al. (2016)

2.2. Spectral preprocessing

The data acquired by the hyperspectral camera are stored in raw digital numbers, and need to be corrected by measuring several reference values without changing the camera's parameters. As suggested by

Suomalainen et al. (2014), in order to reduce the effects of non-uniform lens transmittance and to account for sensor quantum efficiency, the digital number ($\mathbf{DN}$) at each wavelength (λ) should be converted to at-sensor radiance ($\mathbf{L}_{\text{Sample}}$),

$$\mathbf{L}_{\text{Sample}}(\lambda) = \frac{\mathbf{DN}_{\text{Sample}}(\lambda) - \mathbf{DN}_{\text{SampleDarkCurrent}}(\lambda)}{\mathbf{DN}_{\text{FlatField}}(\lambda) - \mathbf{DN}_{\text{FFDarkCurrent}}(\lambda)} \mathbf{L}_{\text{FlatField}(\lambda)} \tag{1}$$

where $\mathbf{DN}_{\text{Sample}}$ and $\mathbf{DN}_{\text{SampleDarkCurrent}}$ are digital number measurements from the sample and nearest (in time) dark current, respectively; and $\mathbf{DN}_{\text{FlatField}}$ and $\mathbf{DN}_{\text{FFDarkCurrent}}$, the digital numbers from flat field and corresponding dark current measurements. An integration sphere with a light level about 95% of saturation was used to provide flat field measurements, also providing internal radiance values ($\mathbf{L}_{\text{FlatField}}$).

Additionally, to obtain accurate sample reflectance measurements, illumination compensation was performed following the "LOGSEP" method described by Drew and Finlayson (2007); Wendel and Underwood (2017b). This compensation procedure makes use of in-field illumination radiance and surface reflectance values for training, and these were taken from the illumination reference panels' mid-grey strip.

2.3. Tree delimitation, mango detection and fruit counting

To accurately obtain all the mango information for each one of the tree sides, an automatic procedure for tree delimitation, mango pixel detection and individual fruit counting was used. Tree delimitation was carried out according to Underwood et al. (2015) and Stein et al. (2016). All trees where segmented within the LIDAR data, which was in turn projected into the camera frames using the methodology from Underwood et al. (2007). In this way, the tree segmentation is transferred to the imagery, to automatically identify which tree is visible in every hyperspectral frame. Fig. 3(a) shows an example of two hyperspectral images of different mango trees in true colour RGB, as segmented automatically by this method. The two images in Fig 3(a) are colour images for human readability, but the full underlying spectra were used in data processing.

A convolutional neural network (CNN) was used as the mango pixel classification model. Classification was performed independently per pixel using the complete spectrum at all available wavelengths, and convolution occurred only along the spectrum and not between adjacent pixels. This differs from typical recent CNN approaches with RGB cameras, where convolutions are performed spatially across regions of adjacent pixels, with just one or three broad spectral bands per pixel. The architecture used for the CNN was based on the two convolutional layer plus two fully connected layers (Fig. 4) model examined by Windrim et al. (2016). For full details of CNN architecture and usage, the reader is encouraged to read Wendel et al. (2018). For each hyperspectral image, each pixel (spectrum) were classified as mango or non-mango by the CNN (Fig. 3(b)), forming binary images with mango pixel detected (Fig. 3(c)).

Finally, from the binary images with mango pixels detected, fruit segmentation was performed, in order to cluster mango pixels and count the number of different mangoes visible in the canopy. Taking as input each binary image (with 0 as non-mango class and 1 as mango pixel), the procedure involved the following sequential steps:

1. Morphological dilation followed by erosion. The structuring element for each operation was parametrised by the choice of either a full rectangle or ellipse, and the corresponding width and height (Fig 3(d)).

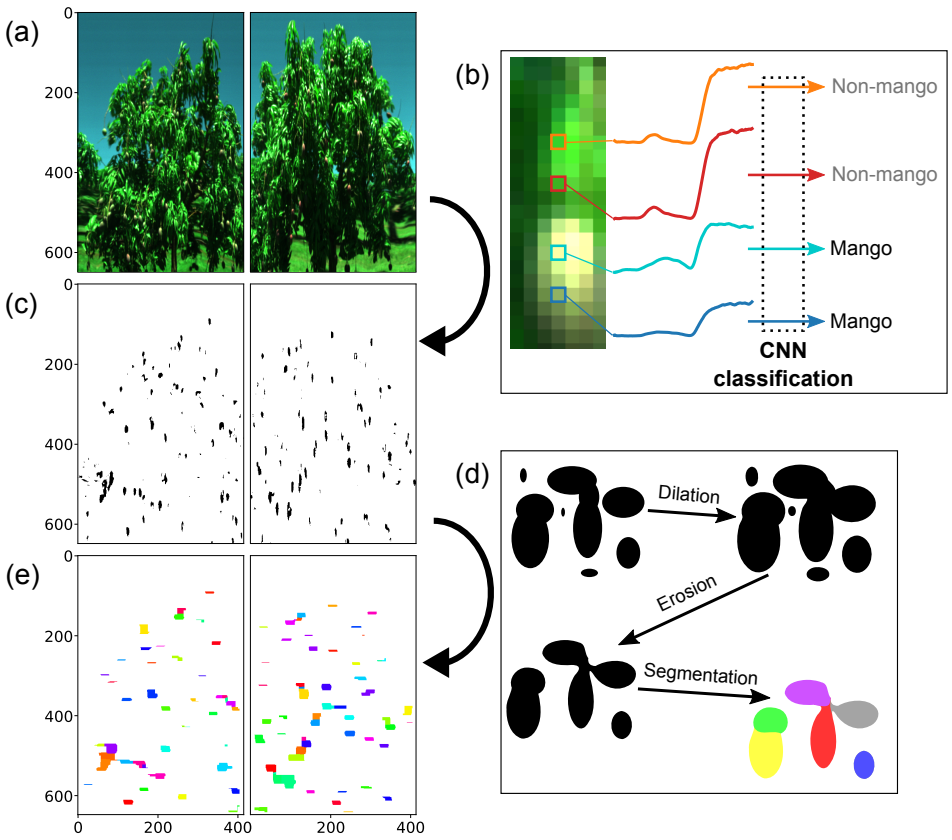

Figure 3: Example of image processing in two different hyperspectral images. These are shown in true colour RGB (a), with the trees delimited and identified in each case. Each hyperspectral pixel (spectrum) is classified as mango or non-mango by a CNN (b), to form a binary image (c). From the binary images, mango pixels are dilated, eroded and segmented (d). From the segmentation, the total number of mangoes in the hyperspectral image can be identified and counted (e). The two images in (a) are colour images for human readability, whereas the full underlying spectra were used in data processing.

2. From this output, the distance transform is computed (the distance from a pixel marked as 1 to its nearest 0) using the Euclidean distance (Paglieroni, 1992).
3. The local maxima were identified, considering local square regions parametrised by width and height values [1]
4. The number of local maxima was used as fruit counting output (Fig. 3(e)).

All the adjustable parameters involved in the described fruit counting steps were selected after an optimisation procedure detailed in the next section.

[1] Steps 2 and 3 are usually carried out immediately before applying marked-based watershed algorithm Roerdink and Meijster (2000), that uses the inverse of the distance transform as input and the local maxima as markers (Bargoti et al., 2015; Stein et al., 2016; Bargoti and Underwood, 2017).

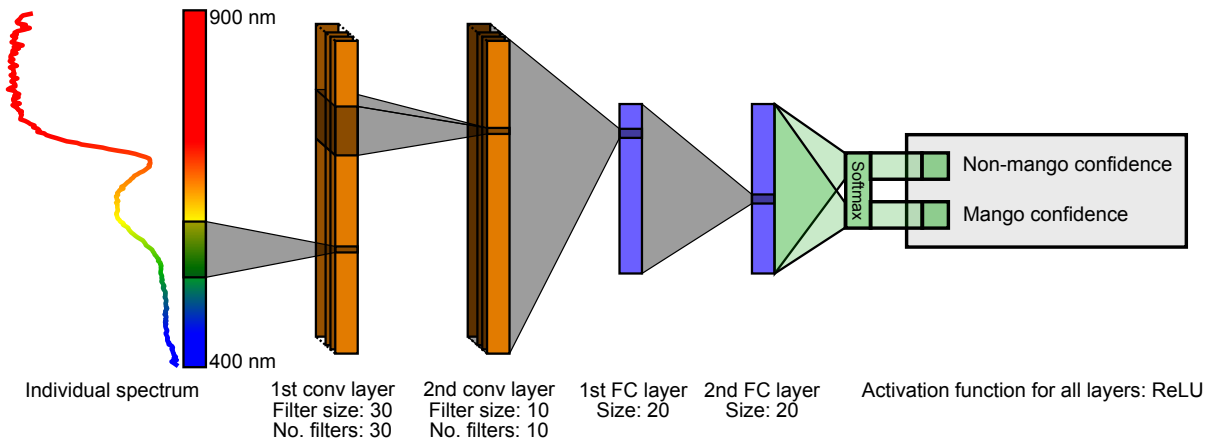

Figure 4: CNN architecture used in this study. The architecture is the two convolutional layer plus two fully connected layer model presented by Windrim et al. (2016). No padding was used for the convolutions. The network provides two outputs representing the softmax "confidence" of mango and non-mango classes.

2.4. Parameter optimisation

Fruit counting makes use of different adjustable parameters that needs to be tuned, as their values influence the final output (the number of mangoes counted). Specifically, these parameters are:

- Dilation structure **width** ($\mathrm{D_w}$), **height** ($\mathrm{D_h}$), $\mathrm{D} \in \mathbb{Z}_{>0}$.
- Erosion structure **width** ($\mathrm{E_w}$), **height** ($\mathrm{E_h}$), $\mathrm{E} \in \mathbb{Z}_{>0}$.
- Structuring elements' **shape** for both morphological operators (S), $\mathrm{S} \in \{\text{rectangle}, \text{ellipse}\}$.
- Local square region **width** ($\mathrm{L_w}$) and **height** ($\mathrm{L_h}$), in local maxima computation, $\mathrm{L} \in \mathbb{Z}_{>0}$.

Therefore, an optimisation process was designed for the parameters set $P = \{\mathrm{D_w}, \mathrm{D_h}, \mathrm{E_w}, \mathrm{E_h}, \mathrm{S}, \mathrm{L_w}, \mathrm{L_h}\}$. The performance was evaluated by applying the morphological operations for fruit counting defined in Section 2.3 to the "field count train" or "RGB train" subsets (described at the beginning of Section 2.1), and finally computing the correlation metrics. As ground truth, each one of these datasets used, respectively, manual mango field counts and RGB counts following the procedure by Stein et al. (2016). Therefore, the optimisation problem was defined as:

$$\arg\max_{P} f(data, \mathrm{D_w}, \mathrm{D_h}, \mathrm{E_w}, \mathrm{E_h}, \mathrm{S}, \mathrm{L_w}, \mathrm{L_h}) \tag{2}$$

where f is an objective function returning R^2 between mango counts and hyperspectral counts given *data* $\in$ {field count train, RGB train} and a parameter set.

Because f is a non-continuous, non-differentiable function, it is not possible to use optimisation methods based on derivatives or gradients. Therefore, evolutionary algorithms were used as metaheuristic to solve the optimisation problem, as they can also work with bounded and constrained parameters, as the ones in P. A genetic algorithm based on CHC (Eshelman, 1991) was developed in Python 2.7.12, adapted

for this problem. CHC algorithm (C standing for cross-generational elitist selection; H for heterogeneous recombination; and the last C for cataclysmic mutation) provides a good trade-off between exploitation (getting as close as possible to a found maxima by incest prevention and elitist selection) and exploration (providing new genetic material when the population has converged too much to explore other maximum).

The algorithm starts with a random population of N individuals and a convergence value δ set to $\frac{|P|}{4}$ that is crossed by randomly picking two parents without replacement, but only allowing the mating if there is enough difference in the parents' genes (avoiding inbreeding). Afterwards, the N best individuals are selected among the union of the original parents and the offspring, and they become the new population. If no offspring was generated (implying that there was low genetic variability in the population), δ is decreased by one, and if it falls bellow zero, a cataclysmic mutation is carried out. This mutation consists on keeping the best individual in the population, adding $N-1$ random individuals, resetting δ to $\frac{|P|}{4}$ and starting over.

Parameters $\{\mathrm{D_w}, \mathrm{E_w}\}$ were coded as genes constrained to positive integers and bounded between 1 and 80, while $\{\mathrm{D_h}, \mathrm{E_h}, \mathrm{L_h}\}$ were positive integers between 1 and 40. On the one hand, the value 80 was selected to prevent excessive mango deformation, and it is two times the average mango height of 40 pixels. On the other hand, the heights were limited to half the maximum width because visible mangoes in hyperspectral images appeared stretched in the vertical dimension due to the relation between the UGV's speed and the camera's frame rate. Local maxima region's width and height, $\{\mathrm{L_w}, \mathrm{L_h}\}$, were bounded between 1 and 80, in order to avoid considering regions beyond two times the average mango height. Following common practices in genetic programming of deriving hyperparameters from problem's constants, the population size was set to 70, ten times the number of genes, and the number of CHC iterations to 280, four times the population size.

2.5. Validation and mapping

From each parameter optimisation performed with "field count train" and "RGB train", the best unique 20 parameter sets from all the iterations, in terms of R^2 values, were selected and considered as models for mango counting using HSI. The unique selection was performed redefining the equality condition between two models. Two models were considered different if, for any of their parameters (excluding the structure shape), their absolute difference surpasses a certain small threshold. This was done because a very small alteration (*e.g.*, one or two units) on any of the width or height parameters—although making the models strictly different—results in a very similar performance.

The performance of mango counting optimised using both field and RGB counts was assessed. For field counts, the 20 best models trained with the "field count train" subset were used to predict the fruit count from the 18 "field count test" trees, computing the determination coefficient (R^2). For RGB counts, the 20 best models trained with the "RGB train" subset were applied to the 215 trees in the "RGB validation" subset, computing the R^2 values for single-, dual- and multi-view. From these results, the model with the highest R^2 (averaged from the three) was selected and applied to the 216 "RGB test" trees. Additionally, these predictions were mapped to illustrate their spatial distribution.

Finally, the hyperspectral images of the "RGB train" subset from the 7th December measurements were processed as described in Sections 2.2 and 2.3, using the best model, to obtain the mango counting in that

date. The outcomes were compared with the results from the 6th December dataset to test the repeatability of the described techniques.

3. Results

3.1. Field count optimised models

The best models from the parameter optimisation using the "field count train" subset are summarised in Table 2, along with their performance when they were applied on the "field count test" subset. Upon optimisation, the R^2_{opt} values reached up to 0.79 ($RMSE_{opt}$ = 34.475 mangoes) in the two first models, that had similar dilation and erosion heights but very different erosion widths.

All the values of D_w lied between 53 and 78, while D_h, L_w and L_h exhibited a larger variability in their values. On the other hand, the erosion's height and width were found to have a highly ranged and balanced distribution between the minimum and maximum values, 5 and 62 for E_w and 1 and 35 for E_h, respectively. For the structuring element's shape for erosion and dilation, both ellipse and square values were equally distributed among the 20 best models. The performance of the parameter sets on the "field count test" subset was very similar to that from optimisation, with R^2_{test} values ranging from 0.71 (model number 19) up to 0.79 (model number 5). Only models 7 and 10, with R^2_{test} of 0.59 and 0.60, respectively, returned discordant statistics (also reflected by the higher $RMSE_{test}$ values, above 50).

The correlation plots for the optimally trained model (first row in Table 2) are presented in Fig. 5. The result from the optimisation, using the "field count train" subset, is shown in Fig. 5(a), while Fig. 5(b) shows the same model applied to the "field count test" subset, yield estimated using the slope intercept equation in 5(a). The train plot displayed a regression line highly tilted toward the horizontal axis, meaning that the hyperspectral counts were well correlated but consistently lower than the actual field counts. Nevertheless, a good fit was present along the regression line, and for this reason, and after correcting with the slope intercept equation, RMSE values resulted in 34.475 and 36.478 mangoes, for train and test subsets respectively.

3.2. RGB count optimised models

After the parameter optimisation was carried out using the 18 trees in the "RGB train" dataset, the results from the 20 best unique models are summarised in Table 3. Determination coefficients were also computed from RGB single-, dual- and multi-view mango count against hyperspectral count. From the optimisation process, R^2_{opt} values ranged from 0.75 to 0.82.

Within the 20 models, all the optimised parameters took a wide range of different values. D_w and L_h obtained mostly high values, up to 75 in both cases. Nevertheless, when compared with results in Table 2, the remaining parameters received values lying in the first half of their domains, with special attention to D_h, that took values below 10, except in four of the models. Again, for the structuring element's shape, both ellipse and square options were almost equally selected. Attending to the statistics from the "RGB validation" subset, R^2 values did not present the same trend of decreasing scores that was observed at optimisation. The model with the highest validation performance in this subset was found not within the first rows in the ranking of Table 3, but in row 13, with scores of 0.77, 0.83 and 0.74 against single-, dual- and multi-view RGB counts, respectively. In almost all the cases, dual-view counts were better predicted

Table 2: Best models from the parameter optimisation using on-tree mango counts, "field count train" subset, and applied to the "field count test" subset.

Rank	R^2_{opt}	$RMSE_{opt}$	D_w	D_h	E_w	E_h	S	L_w	L_h	R^2_{test}	$RMSE_{test}$
1	0.79	34.475	61	35	5	4	square	34	18	0.75	37.435
2	0.79	35.118	75	38	48	3	ellipse	47	24	0.78	35.094
3	0.78	36.197	66	40	62	1	ellipse	48	22	0.75	38.027
4	0.77	37.203	67	34	15	16	square	42	20	0.77	35.971
5	0.75	38.825	71	34	60	26	square	79	19	0.79	33.633
6	0.74	39.687	71	35	47	32	ellipse	29	32	0.78	34.459
7	0.74	39.735	78	39	21	35	ellipse	70	48	0.59	54.758
8	0.74	40.033	59	19	9	10	square	40	53	0.73	39.925
9	0.73	40.831	75	35	62	12	square	49	15	0.79	34.262
10	0.73	40.921	56	38	10	22	ellipse	56	79	0.60	53.853
11	0.73	41.120	73	32	37	3	square	28	49	0.75	37.608
12	0.73	41.534	63	28	45	3	ellipse	56	57	0.72	41.154
13	0.73	41.634	57	32	13	4	square	69	68	0.72	40.974
14	0.73	41.689	57	31	10	16	ellipse	23	12	0.76	36.829
15	0.73	41.745	53	38	52	35	square	36	52	0.73	39.710
16	0.72	42.083	78	28	62	25	ellipse	46	21	0.74	38.382
17	0.72	42.122	69	37	22	16	square	21	47	0.71	42.246
18	0.72	42.539	59	22	42	14	square	56	37	0.74	38.623
19	0.72	42.627	57	32	17	11	ellipse	49	44	0.71	41.506
20	0.72	42.671	75	33	65	29	ellipse	33	25	0.75	38.146

R^2_{opt}: determination coefficient in optimisation (in the "field count train" subset). $RMSE_{opt}$: root-mean-square error in optimisation (in the "field count train" subset). D_w, D_h: Dilation struct width and height. E_w, E_h: Erosion struct width and height. S: Structuring element's shape. L_w, L_h: Local region square's width and height, in local maxima computation. R^2_{test}: determination coefficient when predicting the "field count test" subset. $RMSE_{test}$: root-mean-square error when predicting the "field count test" after applying the slope intercept equation.

than single-view counts, and in turn, these ones were better predicted than the multi-view counts. Only models number 11, 14, 16 and 17 did not follow this behaviour.

3.3. Validation and mapping

The correlation results of model number 13 (Table 3) applied to the "RGB validation" (215 trees) and "RGB test" (216 trees) subsets are plotted in Fig. 6. The plots show correlations against RGB single-view (a, b), dual-view (c, d) and multi-view (e, f). Hyperspectral estimated counts in test plots (b, d, f) were obtained after applying their respective slope intercept equations. The results exhibited virtually identical determination coefficients between each subset, for each RGB view mode. While the determination

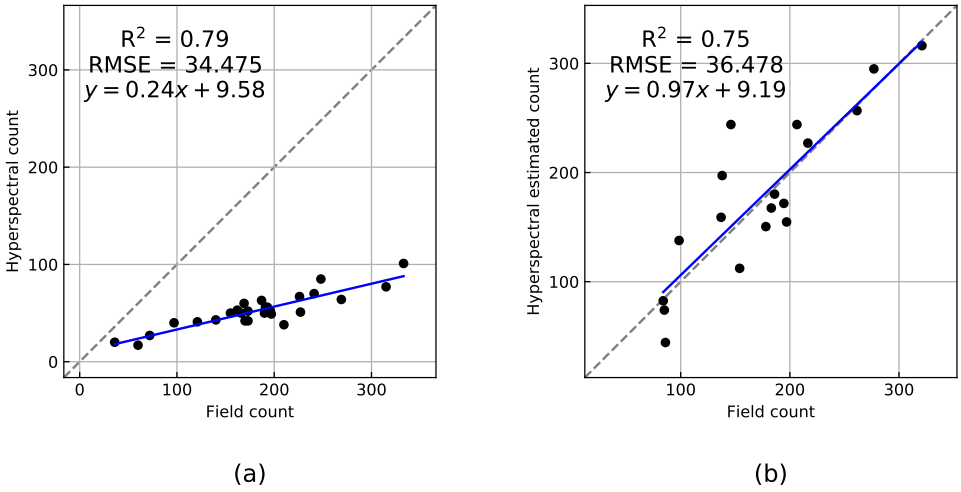

Figure 5: Correlation between field count values (on-tree mango counts) and hyperspectral mango counts in "field count train" (a) and "field count test" (b), using the model number 1 from Table 2. RMSE: root-mean-square error after applying the slope intercept equation.

coefficients were similar for dual- and multi-views, they only differed by one unit in the last figure (0.77 and 0.76) for single-view. As expected by the R^2 scores, RMSE values were also similar between both subsets. As in the results seen in Fig. 5, the regression lines in multi-view train plot (Fig. 6(e)) presented a clear lower gradient, tilting towards the horizontal axis.

As the 216 trees in the "RGB test" subset were not used in any training or validation process, their predictions can be considered as external to the development of the optimised models. These predictions (dual-view counts) were mapped and are presented in Fig. 7. The map showed a high variability in mango yield within the orchard, consistent with the field and RGB observations. Assuming tree rows with Northwest-Southeast orientation, the two central ones presented very different yield predictions on their trees, with high values of 156 mangoes in the left central row and yield below 39 in some trees in the right central row. The two yield basins located at the Southwest and Northeast corners of the orchard could correspond to low values in the surrounding trees reinforced by the fact that few trees were assigned to the "RGB test" subset in those corners, as can be confirmed from Fig. 2.

To test the capability of yield estimation by HSI using models optimised only against RGB data, the parameter set number 13 in 3 was applied to the "field count test" dataset. The scatter plot in Fig. 8 shows the correlation between on-tree mango and hyperspectral counts. A moderately good fit along the regression line is observed (yielding a R^2 of 0.72 and RMSE of 45 mangoes), presenting a low gradient, as field count values were underestimated by HSI.

The repeatability of the whole pipeline for mango yield estimation using HSI was tested by comparing the outcomes from two subsets, "field count train" and "RGB train", in two different dates, 6th and 7th December 2017 (Fig. 9). The parameter sets used were taken from model number 1 (Table 2) and model

Table 3: Best models from the parameter optimisation using RGB single-view counts, "RGB train" subset, and applied to the "RGB validation" subset.

Rank	R^2_{opt}	D_w	D_h	E_w	E_h	S	L_w	L_h	R^2_{Single}	R^2_{Dual}	R^2_{Multi}
1	0.82	57	3	34	16	ellipse	27	58	0.68	0.78	0.68
2	0.80	34	9	20	20	square	10	9	0.74	0.80	0.69
3	0.79	70	4	26	21	square	9	25	0.71	0.77	0.67
4	0.79	31	1	2	14	square	47	6	0.72	0.78	0.68
5	0.78	70	2	6	9	ellipse	8	7	0.72	0.79	0.70
6	0.78	26	9	12	18	square	12	53	0.70	0.77	0.69
7	0.77	33	5	14	16	ellipse	51	15	0.73	0.79	0.72
8	0.77	42	6	35	19	ellipse	31	11	0.72	0.80	0.68
9	0.77	20	11	7	24	square	13	56	0.71	0.79	0.70
10	0.77	70	4	9	21	square	48	34	0.67	0.74	0.63
11	0.77	46	9	29	31	square	51	49	0.64	0.73	0.66
12	0.76	17	24	10	31	square	30	34	0.73	0.80	0.72
13	0.76	46	1	5	7	ellipse	50	16	0.77	0.83	0.74
14	0.76	51	1	4	10	ellipse	6	75	0.69	0.77	0.73
15	0.76	75	1	43	16	square	6	32	0.69	0.76	0.68
16	0.76	41	4	1	27	ellipse	64	35	0.68	0.75	0.70
17	0.75	49	4	44	19	ellipse	73	47	0.65	0.74	0.68
18	0.75	43	9	22	3	square	51	2	0.70	0.76	0.69
19	0.75	59	10	78	9	ellipse	80	16	0.65	0.72	0.61
20	0.75	30	21	23	30	square	16	10	0.73	0.81	0.68

R^2_{opt}: determination coefficient in optimisation (in the "RGB train" subset). D_w, D_h: Dilation struct width and height. E_w, E_h: Erosion struct width and height. S: Structuring element's shape. L_w, L_h: Local region square's width and height, in local maxima computation. The last three columns refer to the determination coefficient obtained when applying the model to the "RGB validation" subset, compared with single-, dual- and multi-view counts.

number 13 (Table 3) respectively. Very close correlations were found in both cases, with R^2 values of 0.88 in field count and 0.91 in RGB subsets. For day 6th and 7th respectively, hyperspectral total counts were 929 and 903 (error of 2.8%, field count) and 15,798 and 15,587 (error of 1.3%, RGB counts).

4. Discussion

This paper presented promising results for extensive in-field prediction of mango yield using an unmanned ground vehicle and hyperspectral imaging. The outcomes from the optimisation of the models provided high precision in the estimation of on-tree mango count, supporting that line-scan HSI can be employed for yield estimation in orchards, and also reliable and accurate predictions when compared with estimations from

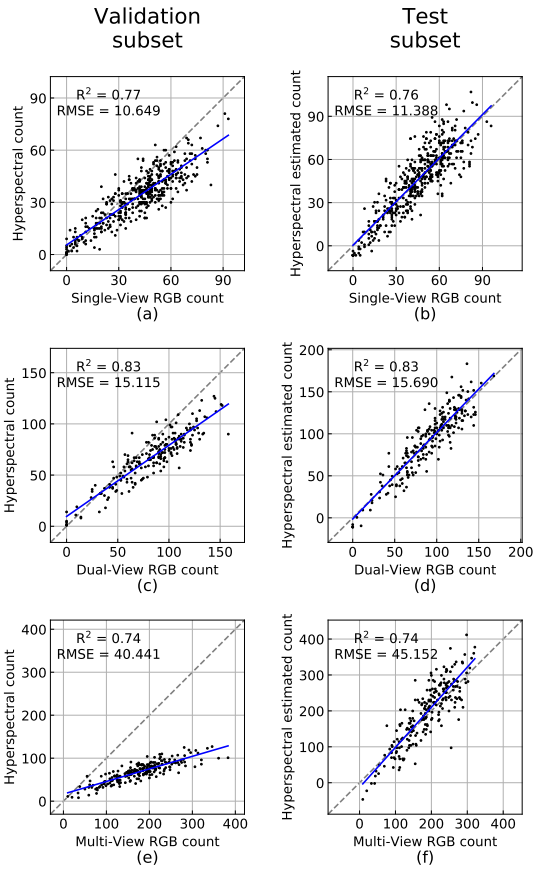

Figure 6: Correlation plots from the orchard block monitoring, comparing RGB counts from single-view (a and b), dual-view (c and d) and multi-view (e and f) with hyperspectral counts from the validation subset (a, c and e) and test subset (b, d, f). Hyperspectral counts where obtained after applying the parameters of the model number 13 in Table 3. RMSE values were obtained after applying the slope intercept equations from the regression line.

RGB techniques that were validated in prior work (Stein et al., 2016). Moreover, the results from the validation on more than two hundred trees, and the testing of the whole pipeline on a further set of two hundred other trees, indicate that the approach is viable in commercial scale orchard blocks.

The determination coefficients in Table 2 showed consistency between the optimisation (R^2_{opt}) and test (R^2_{test}) scores, as they maintained similar determination coefficients, and R^2_{test} also maintained a general descending trend down the ranking. The validation on independent data confirms the appropriateness of the optimised models for yield estimation. Apart from the parameters that specified the width and height of the dilation structuring element (that took values in a relatively close range), no specific pattern could be found in the remaining parameters, that acquired very different options, indicating that the results were not sensitive to the parameter values. This insensitivity to parameter values could imply that the models are more likely to be robust and generalisable, as good outcomes were observed in optimisation (and later confirmed in an independent tree dataset) from very different values.

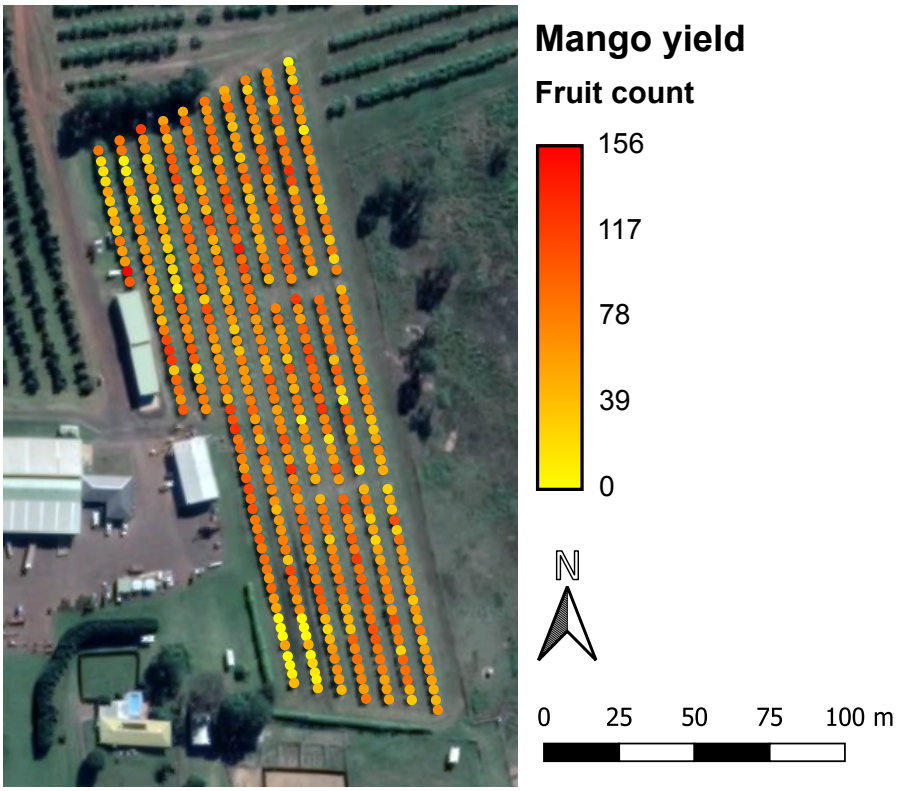

Figure 7: Yield map of the orchard block, coloured by the number of fruit per tree. The map was generated by predicting the RGB dual-view mango counts in all the trees from the orchard block and correcting the predicted values using the slope intercept equation from model number 13 in Table 3. Orthoimagery was collected from *Google Maps*.

The main trait that is observed from Figs. 5 and 8, the low gradient present in the regression lines of the scatter plots, is explained by the fact that the amount of fruit that is visible in the canopy from a lateral point of view is almost always lower than the actual fruit that is present. Particularly in fruit trees, occlusion caused by leaves, branches and other fruit lead to this consequence, as reported by prior work (Bargoti et al., 2015; Bargoti and Underwood, 2016, 2017). This is evident in the graphs presented in Fig. 6, as the HSI results have a slope much closer to unity when compared to the RGB single- or dual-view counts. In other words, single viewpoints from RGB or from a swept line-scan camera unsurprisingly result in a similar degree of undercounting compared to field counts. Yet in both cases the undercounting is consistent and can be compensated by calibration (*i.e.*, correction by the slope-intercept equation). This good fit may be explained by making the assumption that fruit occlusion is present at a constant ratio, and approximately 20 samples in the calibration or training could be sufficient to determine the factor between visible and actual fruit for estimation. Although spectroscopy is able to acquire spectral information from a significantly wider range than RGB cameras, HSI (that ultimately compose a bi-dimensional image) is affected by occlusion in the same way as a regular RGB camera (Stein et al., 2016).

The already developed methodology for mango yield estimation reported by Stein et al. (2016) opened the possibility of computing performance statistics in hundreds of trees from a whole orchard comparing

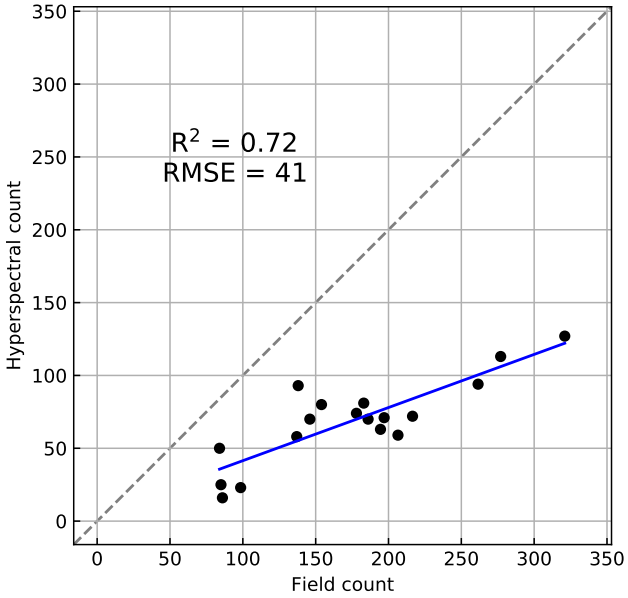

Figure 8: Correlation plot comparing field count values (on-tree mango counts) with hyperspectral counts from the "field count test" subset. Hyperspectral counts where obtained after applying the parameters of the model number 13 in Table 3. RMSE values were obtained after applying the slope intercept equations from the regression line.

HSI to RGB imaging, allowing large independent training, validation and test sets to be used. As exposed in Fig. 6, the very similar R^2 values between validation and test subsets confirmed that the model number 13 (Table 3) was able to build a very consistent generalisation capability, with R^2 scores of 0.77, 0.83 and 0.74 for single-, dual- and multi-view.

The different value ranges that the models' parameters took among the 20 best ones (Table 3) also confirm that results were not sensitive to the parameter values, as in the optimisation against on-tree mango count (the field count subsets). Attending to the determination coefficients obtained from the correlations of the three different RGB fruit count methodologies, the trend described at the end of Section 3.2—correlations with dual-view RGB counts always higher than the ones with single-view—is explained by data aggregation. Dual-view counts (both hyperspectral and RGB) are but the sum of single-view ones from both side of the same tree. This aggregation (like averaging) reduces the magnitude in total of individual errors on either tree side, hence the higher R^2_{Dual} values in Table 3.

The correlation values from the comparison of hyperspectral counts against RGB single-, dual- and multi-view counts indicates that it is not possible to completely reach the same level of accuracy as from RGB cameras and computer vision techniques, especially when R^2_{Multi} is considered. In fact, this was an expected result due to the lower optical features (*i.e.*, lower resolution or limited field of view) commonly offered by hyperspectral cameras. The restriction of line-scan cameras to only one spatial dimension makes it impossible to implement multi-view techniques, which have been shown in prior work to improve accuracy (Moonrinta et al., 2010; Song et al., 2014; Das et al., 2015; Stein et al., 2016). However, the performance

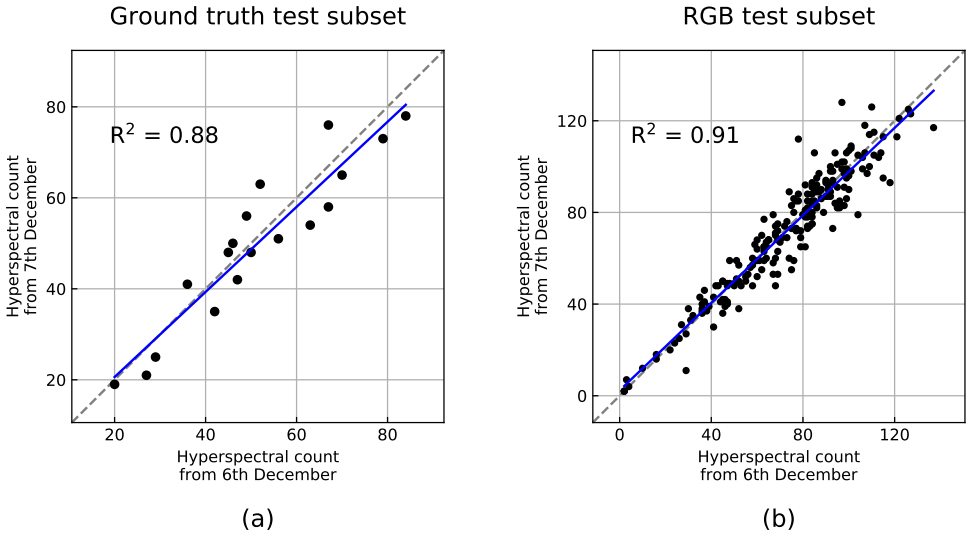

Figure 9: Repeatability of hyperspectral counts on 6th December and 7th December 2017, using model number 1 from Table 2 on the "field count test" subset (a); and model number 13 from Table 3 on the "RGB test" dataset (b). Each dot represent the sum of the mangoes counted in both sides of the same tree (dual view). If single views are independently considered, R^2 values are 0.79 in (a) and 0.85 in (b).

statistics obtained in this paper raises HSI as a feasible alternative for extensive mango yield estimation, particularly in applications where HSI is already (and maybe solely) chosen to detect some other trait.

The methodology followed in this study also allows for the possibility of predicting field count values with a moderately high precision, as shown in Fig. 8 (R^2 of 0.72). This is also reinforced by the similarity to the correlations from the optimisation directly with field counts (5) that, although higher, lied not very far from Fig. 8. It can therefore be implied that the results from automatic monitoring with an UGV and a line-scan hyperspectral camera, exemplified by the yield map in Fig. 7, are reasonably precise for on-tree mango estimation (trained with field counts or RGB data, Tables 2 and 3), accurate for hundreds of trees (Fig. 6) and reliable at different times (Fig. 9).

5. Conclusions

This paper presented a new pipeline for the estimation of mango yield using line-scan hyperspectral imaging acquired from an unmanned ground vehicle in large orchards. The detailed pipeline produced good results ($R^2 \geq 0.75$) using two different ground truth values, and comparable to state-of-the-art RGB techniques. Several steps were followed, from data acquisition, through image processing to model optimisation, and results were tested for both field count values and validated for hundreds of trees compared to state-of-the-art RGB methodologies. Although RGB cameras can be argued as sufficient for automatic fruit counting in orchards, the outcomes from this paper demonstrate that, in scenarios in where HSI is already deployed for the prediction of other nuanced traits, line scan hyperspectral cameras can also deliver accurate estimations of yield, and therefore be extensively used in commercial orchards.

Acknowledgements

Salvador Gutiérrez would like to acknowledge the research funding FPI grant 299/2016 by Universidad de La Rioja, Gobierno de La Rioja. This work is supported by the Australian Centre for Field Robotics (ACFR) at The University of Sydney. Thanks to Simpson Farms for supporting the field work.

References

References

Anderson, N., Underwood, J., Rahman, M., Robson, A., Walsh, K., 2018. Estimation of fruit load in mango orchards: tree sampling considerations and use of machine vision and satellite imagery. Precision Agriculture , 1–17.

Bargoti, S., Underwood, J., 2016. Image classification with orchard metadata, in: Robotics and Automation (ICRA), 2016 IEEE International Conference on, IEEE. pp. 5164–5170.

Bargoti, S., Underwood, J.P., 2017. Image segmentation for fruit detection and yield estimation in apple orchards. Journal of Field Robotics 34, 1039–1060.

Bargoti, S., Underwood, J.P., Nieto, J.I., Sukkarieh, S., 2015. A pipeline for trunk detection in trellis structured apple orchards. Journal of Field Robotics 32, 1075–1094.

Das, J., Cross, G., Qu, C., Makineni, A., Tokekar, P., Mulgaonkar, Y., Kumar, V., 2015. Devices, systems, and methods for automated monitoring enabling precision agriculture, in: Automation Science and Engineering (CASE), 2015 IEEE International Conference on, IEEE. pp. 462–469.

Deery, D., Jimenez-Berni, J., Jones, H., Sirault, X., Furbank, R., 2014. Proximal remote sensing buggies and potential applications for field-based phenotyping. Agronomy 4, 349–379.

Diago, M.P., Fernandes, A.M., Millan, B., Tardaguila, J., Melo-Pinto, P., 2013. Identification of grapevine varieties using leaf spectroscopy and partial least squares. Computers and electronics in agriculture 99, 7–13.

Diago, M.P., Fernández-Novales, J., Fernandes, A.M., Melo-Pinto, P., Tardaguila, J., 2016. Use of visible and short-wave near-infrared hyperspectral imaging to fingerprint anthocyanins in intact grape berries. Journal of agricultural and food chemistry 64, 7658–7666.

Drew, M.S., Finlayson, G.D., 2007. Analytic solution for separating spectra into illumination and surface reflectance components. JOSA A 24, 294–303.

Eshelman, L.J., 1991. The chc adaptive search algorithm: How to have safe search when engaging in nontraditional genetic recombination, in: Foundations of genetic algorithms. Elsevier. volume 1, pp. 265–283.

Gomes, V.M., Fernandes, A.M., Faia, A., Melo-Pinto, P., 2017. Comparison of different approaches for the prediction of sugar content in new vintages of whole port wine grape berries using hyperspectral imaging. Computers and Electronics in Agriculture 140, 244–254.

Gongal, A., Amatya, S., Karkee, M., Zhang, Q., Lewis, K., 2015. Sensors and systems for fruit detection and localization: A review. Computers and Electronics in Agriculture 116, 8–19.

Guo, D., Zhu, Q., Huang, M., Guo, Y., Qin, J., 2017. Model updating for the classification of different varieties of maize seeds from different years by hyperspectral imaging coupled with a pre-labeling method. Computers and Electronics in Agriculture 142, 1–8.

Gutiérrez, S., Fernández-Novales, J., Diago, M.P., Tardaguila, J., 2018. On-the-go hyperspectral imaging under field conditions and machine learning for the classification of grapevine varieties. Frontiers in Plant Science 9, 1102.

Ishida, T., Kurihara, J., Viray, F.A., Namuco, S.B., Paringit, E.C., Perez, G.J., Takahashi, Y., Marciano, J.J., 2018. A novel approach for vegetation classification using uav-based hyperspectral imaging. Computers and Electronics in Agriculture 144, 80–85.

Lu, J., Zhou, M., Gao, Y., Jiang, H., 2017. Using hyperspectral imaging to discriminate yellow leaf curl disease in tomato leaves. Precision Agriculture , 1–16.

Ma, T., Li, X., Inagaki, T., Yang, H., Tsuchikawa, S., 2018. Noncontact evaluation of soluble solids content in apples by near-infrared hyperspectral imaging. Journal of Food Engineering 224, 53–61.

Moonrinta, J., Chaivivatrakul, S., Dailey, M.N., Ekpanyapong, M., 2010. Fruit detection, tracking, and 3d reconstruction for crop mapping and yield estimation, in: Control Automation Robotics & Vision (ICARCV), 2010 11th International Conference on, IEEE. pp. 1181–1186.

Oldeland, J., Dorigo, W., Lieckfeld, L., Lucieer, A., Jürgens, N., 2010. Combining vegetation indices, constrained ordination and fuzzy classification for mapping semi-natural vegetation units from hyperspectral imagery. Remote Sensing of Environment 114, 1155–1166.

Paglieroni, D.W., 1992. Distance transforms: Properties and machine vision applications. CVGIP: Graphical models and image processing 54, 56–74.

Park, B., Lu, R., 2015. Hyperspectral imaging technology in food and agriculture. Springer.

Payne, A., Walsh, K., 2014. Machine vision in estimation of fruit crop yield. Plant Image Analysis: Fundamentals and Applications; CRC Press: Boca Raton, FL, USA , 329–374.

Payne, A.B., Walsh, K.B., Subedi, P., Jarvis, D., 2013. Estimation of mango crop yield using image analysis–segmentation method. Computers and electronics in agriculture 91, 57–64.

Pu, Y.Y., Sun, D.W., 2015. Vis–nir hyperspectral imaging in visualizing moisture distribution of mango slices during microwave-vacuum drying. Food chemistry 188, 271–278.

Qureshi, W., Payne, A., Walsh, K., Linker, R., Cohen, O., Dailey, M., 2017. Machine vision for counting fruit on mango tree canopies. Precision Agriculture 18, 224–244.

Roerdink, J.B., Meijster, A., 2000. The watershed transform: Definitions, algorithms and parallelization strategies. Fundamenta informaticae 41, 187–228.

Rungpichayapichet, P., Nagle, M., Yuwanbun, P., Khuwijitjaru, P., Mahayothee, B., Müller, J., 2017. Prediction mapping of physicochemical properties in mango by hyperspectral imaging. Biosystems Engineering 159, 109–120.

Song, Y., Glasbey, C., Horgan, G., Polder, G., Dieleman, J., Van der Heijden, G., 2014. Automatic fruit recognition and counting from multiple images. Biosystems Engineering 118, 203–215.

Stein, M., Bargoti, S., Underwood, J., 2016. Image based mango fruit detection, localisation and yield estimation using multiple view geometry. Sensors 16, 1915.

Sun, D.W., 2010. Hyperspectral imaging for food quality analysis and control. Elsevier.

Suomalainen, J., Anders, N., Iqbal, S., Roerink, G., Franke, J., Wenting, P., Hünniger, D., Bartholomeus, H., Becker, R., Kooistra, L., 2014. A lightweight hyperspectral mapping system and photogrammetric processing chain for unmanned aerial vehicles. Remote Sensing 6, 11013–11030.

Thomas, S., Behmann, J., Steier, A., Kraska, T., Muller, O., Rascher, U., Mahlein, A.K., 2018. Quantitative assessment of disease severity and rating of barley cultivars based on hyperspectral imaging in a non-invasive, automated phenotyping platform. Plant methods 14, 45.

Tian, X., Li, J., Wang, Q., Fan, S., Huang, W., 2018. A bi-layer model for nondestructive prediction of soluble solids content in apple based on reflectance spectra and peel pigments. Food chemistry 239, 1055–1063.

Underwood, J., Scheding, S., Ramos, F., 2007. Real-time map building with uncertainty using colour camera and scanning laser, in: Proceedings of the 2007 Australasian Conference on Robotics and Automation, Citeseer. pp. 1330–1334.

Underwood, J., Wendel, A., Schofield, B., McMurray, L., Kimber, R., 2017. Efficient in-field plant phenomics for row-crops with an autonomous ground vehicle. Journal of Field Robotics 34, 1061–1083.

Underwood, J.P., Jagbrant, G., Nieto, J.I., Sukkarieh, S., 2015. Lidar-based tree recognition and platform localization in orchards. Journal of Field Robotics 32, 1056–1074.

Uto, K., Seki, H., Saito, G., Kosugi, Y., 2013. Characterization of rice paddies by a uav-mounted miniature hyperspectral sensor system. IEEE Journal of Selected Topics in Applied Earth Observations and Remote Sensing 6, 851–860.

Wang, Y., Hu, X., Hou, Z., Ning, J., Zhang, Z., 2018. Discrimination of nitrogen fertilizer levels of tea plant (camellia sinensis) based on hyperspectral imaging. Journal of the Science of Food and Agriculture .

Wang, Z., Walsh, K.B., Verma, B., 2017. On-tree mango fruit size estimation using RGB-D images. Sensors 17, 2738.

Wendel, A., Underwood, J., 2016. Self-supervised weed detection in vegetable crops using ground based hyperspectral imaging, in: Robotics and Automation (ICRA), 2016 IEEE International Conference on, IEEE. pp. 5128–5135.

Wendel, A., Underwood, J., 2017a. Extrinsic parameter calibration for line scanning cameras on ground vehicles with navigation systems using a calibration pattern. Sensors 17, 2491.

Wendel, A., Underwood, J., 2017b. Illumination compensation in ground based hyperspectral imaging. ISPRS Journal of

Photogrammetry and Remote Sensing 129, 162–178.

Wendel, A., Underwood, J., Walsh, K., 2018. Maturity estimation of mangoes using hyperspectral imaging from a ground based mobile platform. Computers and Electronics in Agriculture 155, 298–313.

Windrim, L., Ramakrishnan, R., Melkumyan, A., Murphy, R., 2016. Hyperspectral CNN classification with limited training samples. arXiv preprint arXiv:1611.09007 .

Yang, C., Everitt, J.H., Bradford, J.M., Murden, D., 2004. Airborne hyperspectral imagery and yield monitor data for mapping cotton yield variability. Precision Agriculture 5, 445–461.

Yue, J., Yang, G., Li, C., Li, Z., Wang, Y., Feng, H., Xu, B., 2017. Estimation of winter wheat above-ground biomass using unmanned aerial vehicle-based snapshot hyperspectral sensor and crop height improved models. Remote Sensing 9, 708.

Zhang, X., Liao, C., Li, J., Sun, Q., 2013. Fractional vegetation cover estimation in arid and semi-arid environments using hj-1 satellite hyperspectral data. International Journal of Applied Earth Observation and Geoinformation 21, 506–512.

Zhou, K., Cheng, T., Zhu, Y., Cao, W., Ustin, S.L., Zheng, H., Yao, X., Tian, Y., 2018. Assessing the impact of spatial resolution on the estimation of leaf nitrogen concentration over the full season of paddy rice using near-surface imaging spectroscopy data. Frontiers in plant science 9.